

Wake behind a concave curved cylinder

Fengjian Jiang,¹ Bjørnar Pettersen,¹ Helge I. Andersson,² Jongmin Kim,³ and Sungtae Kim³

¹*Department of Marine Technology, Norwegian University of Science and Technology (NTNU), NO-7491, Trondheim, Norway*

²*Department of Energy and Processing Engineering, NTNU, NO-7491, Trondheim, Norway*

³*R&D Center UIT Solutions, 110 Yeoksam-ro, Gangnam-gu, Seoul 06252, Republic of Korea*



(Received 17 April 2018; published 18 September 2018)

The wake behind a quarter-of-ring concave curved cylinder is investigated in this paper by means of direct numerical simulations. The plane of curvature is aligned with the uniform incoming flow. We have appended straight extensions to both ends of the curved part of the cylinder, such that free ends are eliminated from the simulations. The effect of the *vertical extension*, i.e., the straight extension with its axis normal to the inflow, is carefully studied and turns out to be significant. The results from several different Reynolds numbers ($Re = 100\text{--}500$) are presented, from which a clear picture of the wake transition behind this configuration could be sketched. The concave curved cylinder wake consists of different flow regimes along the span. Oblique shedding, vortex dislocations, and various shedding frequencies are captured in different flow regimes. At $Re \leq 300$, the flow regimes change abruptly, but at $Re = 400$ and 500 , the changes are continuous, so the boundaries between them are difficult to observe. A frequency band, instead of one single dominating frequency, manifests itself in the three-dimensional (3D) energy spectrum.

DOI: [10.1103/PhysRevFluids.3.094804](https://doi.org/10.1103/PhysRevFluids.3.094804)

I. INTRODUCTION

A. The curved cylinder wake

As a commonly encountered configuration in many engineering applications, a curved cylinder is specially favored by the engineers in the marine and offshore community, where we have catenary risers hanging in the sea, pipelines laying on the seabed bended in all directions, anchor lines, etc. Most of these examples are from underwater installations, under which context the dynamics of the curved cylinder structures are heavily affected by the currents in the ocean, generating complex wakes which apparently need special considerations in the design phase. However, our understanding of the curved cylinder wake is still limited, mostly due to the complexity of the flow.

Unlike the well-addressed straight circular cylinder wake, to define a curved cylinder configuration is more complicated. In addition to the cylinder diameter and fluid-cylinder relative speed, the radius of curvature and the flow direction also become dominating control parameters. As reviewed in Ref. [1], the early research on the curved cylinder wake mostly considered the flow normal to the plane of curvature; see, e.g., Ref. [2].

References [3,4] were among the first to investigate the curved cylinder wake when the incoming flow direction is in the plane of curvature. Reference [4] was probably the first that comprehensively compared the wake of two different curved cylinder configurations with the flow in the plane of curvature. The two configurations were referred to as *convex* and *concave curved cylinder*, respectively. A configuration is called convex when the flow is towards the outer face of the curved cylinder, while the concave configuration has the opposite flow direction.

Reference [4] showed the distinctly different features between the convex and concave curved cylinder wakes at $Re = 100$ and 500 . In the convex case, the vortex shedding is slightly curved

following the curved span, while in the concave curved cylinder wake, the vortex shedding is heavily suppressed by the axial flow at the leeward side. Reference [1] investigated the convex curved cylinder configuration and for the first time reported the turbulent wake behind it. The concave curved cylinder wake is, on the other hand, more complex, and only more recently have researchers described this wake in detail.

Reference [5] reported a series of experiments of two concave curved cylinders with different curvatures at Reynolds numbers lower than 916 and carefully studied the wakes behind them. While they kept the incoming flow towards the inner face of the curved cylinder, different inflow angles were considered. In their work, they concluded that the concave curved cylinder wake has distinctly different flow regimes. Regime 1 is the nonshedding regime dominated by a counter-rotating vortex pair. Regime 2 has oblique shedding and a low dominating frequency. Regime 3 is the normal vortex shedding regime with a higher dominating frequency, while regime 4 is another nonshedding regime with streamwise vortices. Similar flow regimes were previously proposed for the wake behind an inclined straight cylinder in Ref. [6]. The oblique shedding is also known from straight cylinder wakes. It is caused by end effects (3D effect) in experiments, and the frequency of the oblique shedding is directly related to the oblique angle [7]. When oblique shedding happens, the 3D instability of the cylinder wake, i.e., the well-known mode A and mode B, will be postponed [8]. The oblique shedding in a concave curved cylinder wake is otherwise caused by the strong axial flow along the curved span. To what extent this axial flow affects the overall wake has not been studied before.

Oblique and cellular vortex shedding in wakes behind straight cylinders with a spanwise nonuniformity has been extensively studied; see e.g., Ref. [9] and references therein. The two most prominent configurations are (1) a uniform circular cylinder in shear flow [10] and (2) a tapered cylinder in uniform flow [11]. One can postulate an analogy between these two configurations and the wake behind a curved cylinder by assuming the shedding frequency to be given as $f = St U_0 \sin \theta / D$. The shedding frequency varies along the span of the cylinder if either (1) the incoming velocity U_0 or (2) the diameter D or (3) the angle θ between the inflow and the cylinder axis (see Fig. 1) varies along the span. The envisaged frequency variation may lead to oblique and/or cellular vortex shedding. The analogy between variable U_0 and variable D was addressed in Ref. [9], whereas the hypothesized analogy also with variable θ , i.e., a curved cylinder, has not been examined so far.

Aside from the wake studies, there are also some experimental studies focused on free-oscillating curved cylinders, which is more related to vortex-induced vibration (VIV) problems. Since VIV is out of the scope of the present study, interested readers are directed to Refs. [12–14] and the relevant references therein.

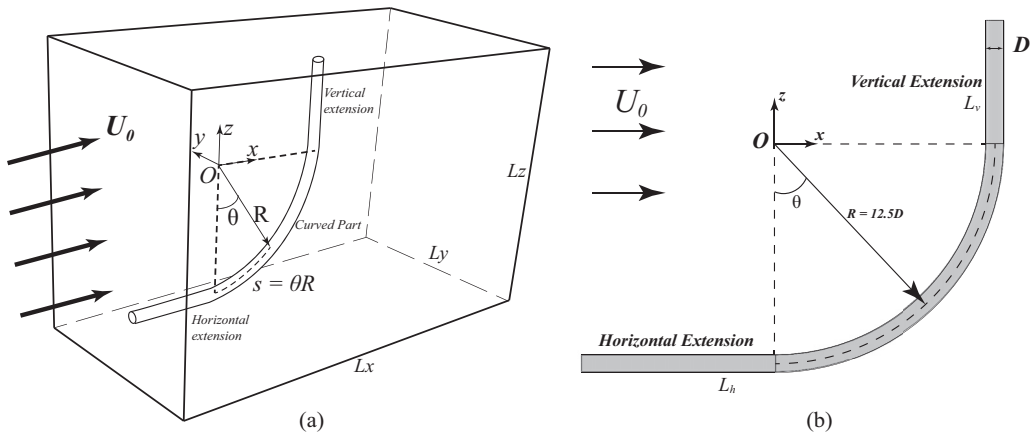


FIG. 1. (a) Three-dimensional computational domain for the concave cylinder configuration. Notice the domain is not to scale. (b) Projection sketch of the geometry in the symmetry plane, the (x, z) plane at $y/D = 0$. The origin of the configuration is marked as O .

B. Computational issues

Differently from the experimental study [5], where free ends (and free surface) show up, the previous numerical studies all try to avoid free ends in the simulations and accordingly have special considerations of the boundary conditions. Therefore, straight extensions are usually used in the numerical studies. Depending on their axial directions, we refer to them as the *vertical* and *horizontal extension*, respectively. Some numerical aspects for curved cylinder wake simulations have been addressed in earlier studies, for both convex and concave configurations.

The horizontal extension has its span aligned with the incoming flow and is adopted to get rid of the free ends in the computational domain. Therefore, a horizontal extension is normally extended all the way to the outlet (for convex configuration) or the inlet (for concave configuration) of the computational domain (see the examples in Refs. [15,16], respectively). In a convex curved cylinder simulation, the length of the horizontal extension L_h is simply determined by the size of the computational domain. In a concave curved cylinder wake, however, we also need to consider the interaction between the horizontal extension and the inlet boundary. The influence of L_h for a concave configuration was carefully studied in Ref. [16], in which the authors suggested $L_h = 10D$ to be a minimum choice.

The vertical extension has its span normal to the incoming flow, and it has been used to reduce the influence of the free-slip boundary at the upper end of the configuration. Reference [4] first considered this extension and used a $6D$ -long vertical extension, i.e., $L_v = 6D$. Reference [15] was a careful study of the length effects of the vertical extension for a *convex* curved cylinder. However, the length effects of the vertical extension for a *concave* curved cylinder wake has never been addressed before.

In addition to the numerical considerations, we should also keep in mind that straight extensions are relevant and important in real-life engineering applications. The curved cylinder part rarely appears isolated in an installation. No matter whether in a hanging riser or in a pipeline system, the curved part is usually connected with straight extensions. Therefore, to treat the curved cylinder together with its straight extensions as one object also offers more practical information for the real-life configurations. For this reason, we first aim to carefully study the length effect of the vertical extension in the present study, by means of direct numerical simulations. Second, we will investigate the wake transition of a concave curved cylinder as the Reynolds number increases.

II. FLOW PROBLEM AND COMPUTATIONAL ASPECTS

A. Flow configuration

We consider a quarter-of-ring curved cylinder whose diameter is D , and the radius of the ring (curvature) is $R = 12.5D$. The geometry is adopted from the previous study [4]. The concave configuration will be studied, i.e., the free-stream is directed towards the inner face of the ring. The flow configuration defined in the present study is shown in Fig. 1(a), while the geometry in the symmetry plane is depicted in Fig. 1(b). The Reynolds number is defined based on the free-stream velocity U_0 and cylinder diameter D , i.e., $Re = U_0 D / \nu$, where ν is the kinematic fluid viscosity. In this study, we investigate the wake behind this configuration for Reynolds numbers ranging from $Re = 100$ to 500 .

We hereby define the streamwise direction as the x direction, crossflow direction as the y direction, and the vertical direction as the z direction. The origin O is located at the center of the curvature, as shown in Fig. 1. The computational domain has dimensions of L_x , L_y , and L_z in the respective directions. The boundary conditions defined in the simulations are listed below:

Inlet boundary: uniform free stream, i.e., $u_i = (u, v, w) = (U_0, 0, 0)$

Outlet boundary: Neumann boundary conditions for the velocity components ($\partial u / \partial x = \partial v / \partial x = \partial w / \partial x = 0$) and zero pressure ($p = 0$)

Two vertical side boundaries normal to the y direction: free-slip boundaries, i.e., $v = 0$, and $\partial u/\partial y = \partial w/\partial y = 0$

Two horizontal side boundaries normal to the z direction: free-slip boundaries, i.e., $w = 0$, and $\partial u/\partial z = \partial v/\partial z = 0$

The surface of the cylinder is treated as a no-slip and impermeable wall.

As depicted in Fig. 1, straight extensions were appended to the two ends of the quarter-ring, as already mentioned in the Introduction. The horizontal extension length $L_h = 10D$, as suggested in Ref. [16] for the same configuration, is fixed for all simulations. The vertical extension length L_v , however, will be given different values, in order to study its effect on the wake. A list of the parameters of all the DNS simulations in this study is presented in Table I. It is noteworthy that, unlike Refs. [4,16], a boundary layer profile around the cylinder cross section at the inlet boundary is not prescribed in the present study. Because we have examined, through a test case, that an inflow boundary layer around the cylinder at the inlet has a negligible influence on the flow when the horizontal extension is $10D$ long.

B. Numerical methods

In our DNS study, the time-dependent full Navier-Stokes equations for incompressible fluid are directly solved:

$$\frac{\partial u_i}{\partial x_i} = 0 \quad (1)$$

$$\frac{\partial u_i}{\partial t} + u_j \frac{\partial u_i}{\partial x_j} = -\frac{1}{\rho} \frac{\partial p}{\partial x_i} + \nu \frac{\partial^2 u_i}{\partial x_j \partial x_j} \quad (2)$$

A well-verified second-order finite volume DNS/LES code MGLET [17] was utilized to conduct all the simulations. In MGLET, Eqs. (1) and (2) are discretized on 3D staggered Cartesian grids.

TABLE I. Detailed information of all simulations.

Purpose	Case	Re	Min grid size (Δ/D)	Vertical extension length (L_v/D)	Domain size ($L_x/D \times L_y/D \times L_z/D$)	Total number of grid points (million)
Grid independence study (GI series)	GI-coarse	500	0.03	18	$46.08 \times 34.56 \times 57.6$	110
	GI-medium	500	0.02	18	$51.2 \times 38.4 \times 51.2$	221
	GI-fine	500	0.015	18	$46.08 \times 34.56 \times 57.6$	407
	GI-fine2	500	0.0125	18	$56.0 \times 33.6 \times 56.0$	1040
	GI-400m	400	0.02	24	$51.2 \times 38.4 \times 51.2$	257
	GI-400f	400	0.015	24	$46.08 \times 34.56 \times 57.6$	460
Vertical extension study (VE series)	VE-0D	200	0.02	0	$51.2 \times 38.4 \times 25.6$	109
	VE-6D	200	0.02	6	$51.2 \times 38.4 \times 38.4$	146
	VE-12D	200	0.02	12	$51.2 \times 38.4 \times 38.4$	182
	VE-18D	200	0.02	18	$51.2 \times 38.4 \times 51.2$	221
	VE-21D	200	0.02	21	$51.2 \times 38.4 \times 51.2$	239
	VE-24D	200	0.02	24	$51.2 \times 38.4 \times 51.2$	257
Wake study (Re series)	RE-100	100	0.02	24	$51.2 \times 38.4 \times 51.2$	257
	RE-200	200	0.02	24	$51.2 \times 38.4 \times 51.2$	257
	RE-300	300	0.02	24	$51.2 \times 38.4 \times 51.2$	257
	RE-400	400	0.02	24	$51.2 \times 38.4 \times 51.2$	257
	RE-500	500	0.015	24	$48.0 \times 38.4 \times 57.6$	637

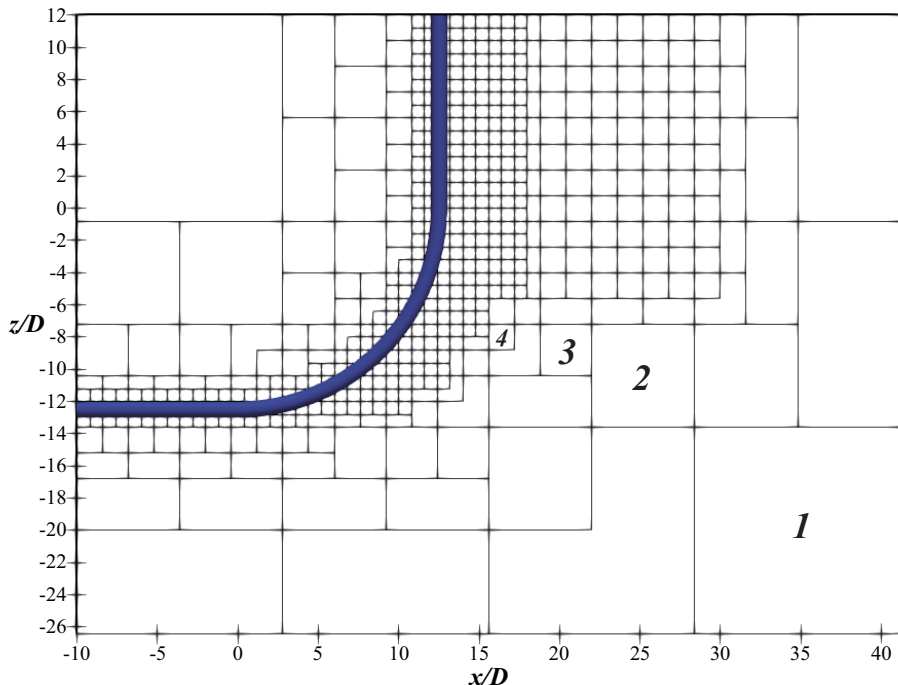


FIG. 2. An example (case VE-12D) of the multilevel grids. The slice of the grid box distribution in the symmetry plane, i.e., the (x, z) plane at $y/D = 0$, is shown. Each square represents a 3D grid box, while each grid box, regardless of its size, contains the same amount ($N \times N \times N$) of grid cells. Therefore, the square size also indicates the different levels of grid resolution. One can find five levels of grids, among which the first four levels are indicated with numbers.

The discretized equations are integrated in time with Williamson's third-order Runge-Kutta scheme [18], while pressure corrections are achieved by Stone's strongly implicit procedure (SIP) [19]. The representation of the cylindrical geometry inside the Cartesian grid is accomplished by an immersed boundary method (IBM). The details of this IBM and its validation can be found in Ref. [20]. The same code has recently been used for DNS of wake flow with the same geometry [1,16].

A local grid refinement method [21] is utilized in the gridding process of all the computational cases listed in Table I. The mesh is constructed by cubic Cartesian grid boxes, in each of which $N \times N \times N$ Cartesian grid cells are uniformly distributed. In the interesting regions (such as regions close to the geometry, and where complex flow phenomena take place), the grid boxes are locally refined by splitting each of them further into eight child boxes. Each child box holds the same amount of uniformly distributed grid cells ($N \times N \times N$) as the grid box before refinement (parent box). In other words, the grid resolution on a child level is two times finer than that on the parent level. In the cases listed in Table I, depending on the different minimum grid size Δ , a mesh may have four to six levels of grids. Figure 2 gives an impression of the multigrid hierarchy by showing the grid box distributions in the symmetry plane.

It is noteworthy that, due to the use of multilevel grids, the computational domain size must be adjusted to an integer number times the size of the coarsest grid box (decided by the grid size in the coarsest level and N) and therefore may not be an integer. In Table I, one may also notice the identical L_z for cases VE-18D, VE-21D, and VE-24D, despite the different vertical extension lengths. This is because even in case VE-24D, the distance between the lower edge of the cylinder and the bottom boundary layer is $24.2D$ and already larger than in earlier studies [1,16]. Therefore, we claim that the blockage effect is negligibly small.

TABLE II. Force coefficients for grid independence study. Note that the four first columns are for simulations at $\text{Re} = 500$ whereas the two last columns are for simulations at $\text{Re} = 400$. Numerical specifications are provided in Table I.

Cases	GI-coarse	GI-medium	GI-fine	GI-fine2	GI-400m	GI-400f
C_{F_x-m}	0.901	0.887	0.884	0.884	0.945	0.941
C_{F_y-rms}	0.0330	0.0311	0.0306	0.0305	0.0452	0.0447

C. Grid refinement study

As listed in Table I, we choose the largest Reynolds number considered in this study, i.e., $\text{Re} = 500$, for the grid independence test. Four different meshes were generated: GI-coarse, GI-medium, GI-fine, and GI-fine2. The vertical extension $L_v = 18D$ was fixed in the grid independence test, the reason for this choice will be further discussed in the next section. Here we compare the results from the four different meshes. Each of the four cases has been run for at least 900 time units ($900D/U_0$), in order to let the flow develop properly.

Table II lists the time-averaged drag coefficient (C_{F_x-m}) and the root mean square of the side force coefficient (C_{F_y-rms}) obtained from the four simulations. Note that the time-averaged side force is zero in all simulations. The drag force and side force are captured for the whole geometry, i.e., including both vertical and horizontal extensions, and the coefficients were normalized by the inflow velocity and projected area ($S_p = 31D^2$ for $\text{Re} = 500$ grid test; $S_p = 37D^2$ for $\text{Re} = 400$ grid test), as

$$C_F = F / 0.5 \rho U_0^2 S_p. \quad (3)$$

From the data in Table II, we notice that except for case GI-coarse, the other three cases all produce very similar results both for C_{F_x-m} and C_{F_y-rms} , which strongly indicate that the last three meshes for $\text{Re} = 500$ produce very similar solutions of the wake flow. In Fig. 3(a) we plot the mean axial velocity along a concentric arc of the curved part of the cylinder in the symmetry plane, $1D$ from the leeward face of the cylinder. The location of this concentric arc is shown in Fig. 3(b). Since this concentric arc is located close to the geometry, the local tangential velocity represents the axial flow and is calculated based on the time-averaged streamwise velocity $\langle u \rangle$ and vertical velocity $\langle w \rangle$, as also sketched in Fig. 3(b). The abscissa is measured by the angle θ , defined in Fig. 3(b). We would like to mention here, that the time-averaged cross-flow velocity $\langle v \rangle$ is zero everywhere in the symmetry plane, which is in agreement with the zero mean side force mentioned above. Moreover, the axial velocity u_{ax} slightly exceeds U_0 as $\theta \rightarrow 0^\circ$ in Fig. 3. This indicates a modest blockage effect even though the distance between the horizontal part of the cylinder and the free-slip boundary at the bottom of the computational domain exceeds $20D$. However, the $<2\%$ blockage is negligibly small for all practical purposes. On the other hand, the substantial u_{ax} as $\theta \rightarrow 90^\circ$ reflects a nonzero vertical velocity, which is typical for oblique vortex shedding, as discussed in Refs. [9,10].

In Fig. 3(a) we observe that the four velocity distributions from the grid studies show the same trends. Only when it comes to the end, i.e., at the interface of the curved part of the cylinder and the vertical extension, can we see different trends. Similar as what was presented in Table II, the GI-coarse case shows the largest deviation from the other three cases, indicating that the coarsest mesh is not sufficiently fine to give reliable results. Aside from that, the distributions for GI-medium, GI-fine, and GI-fine2 show good agreements with each other. We could barely observe any differences between the results from GI-fine and GI-fine2.

The data in Table II shows that the computed force coefficients for the GI-fine and GI-fine2 meshes are accurate to within 2%, and the axial velocity variations in Fig. 3 are indistinguishable. However, for a DNS simulation, a small drop in the minimum grid size Δ leads to large increase in the total number of grid points. For instance, the total number of grid points in the GI-fine2 case

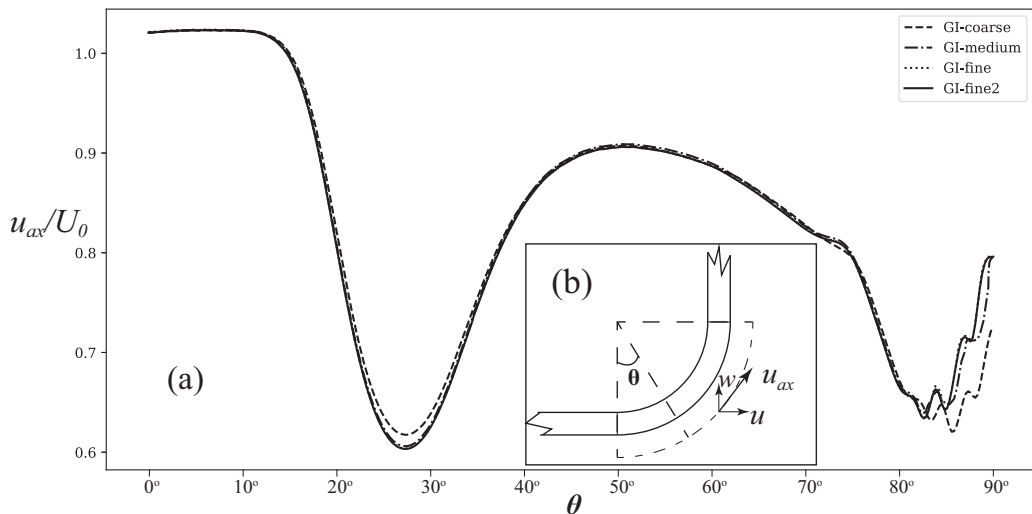


FIG. 3. (a) The mean axial velocity u_{ax}/U_0 plotted along a concentric arc of the curved cylinder whose radius is $14D$, i.e., $1D$ behind the leeward face of the curved cylinder. Results from cases GI-coarse, GI-medium, GI-fine, and GI-fine2 are plotted. (b) The curved dashed line indicates the concentric arc along which the mean axial velocities in (a) are plotted. $Re = 500$. The physical interpretation of the peculiar variation of the axial velocity is deferred to the discussion concerning Fig. 7 in Sec. III.

is twice that of GI-fine and amounts to more than 10^9 grid points. Considering that GI-fine2 and GI-fine give almost identical results, the GI-fine2 mesh is apparently over-refined. Since we aim to run the simulations longer for later discussions, GI-fine has been chosen as the final mesh for the highest $Re (= 500)$ considered in this study.

The very small discrepancy between GI-fine and GI-medium at $Re = 500$ makes it reasonable to assume that the mesh for GI-medium may be sufficiently fine to resolve the wake at a lower $Re = 400$. For this reason, we conducted another grid independence study for $Re = 400$, indicated as GI-400m and GI-400f in Table I. The force coefficients from GI-400m and GI-400f were also shown in Table II. The results indicate that the minimum grid size $\Delta = 0.02D$ gives satisfactory results. The mesh size for GI-400m is acceptable for performing series of simulations and is therefore adopted for all lower Reynolds numbers ($Re \leq 300$) without any further grid studies.

III. INFLUENCE OF THE VERTICAL EXTENSION

In this section, we present the results from a detailed study of the influence of the vertical extension. Six different vertical extension lengths ($L_v/D = 0, 6, 12, 18, 21, 24$) were selected. The information of these six cases are listed in Table I, as the “VE series.” To avoid any other influences aside from the vertical extension, we fixed $Re = 200$ and used the same mesh for the curved cylinder part in this series of simulations. The mesh topology in the (x, y) plane for the vertical extension is also fixed, so that the only difference between the six cases is the length L_v .

Figure 4 shows the overall wake structures from all six VE simulations. The iso-surface of $\lambda_2 = -0.01$ [22] is adopted to demonstrate the different wake structures. A direct comparison between Figs. 4(a) and 4(f) show the strong effect of the vertical extension on the wake behind the total configuration.

In Figs. 4(a) and 4(b), we could not observe any vortex shedding, The results in Fig. 4(a) is similar as what was shown in Ref. [4] for the same configuration but at $Re = 100$ (see Fig. 11 in their paper). The vortex shedding is heavily suppressed by the axial flow behind the cylinder. The

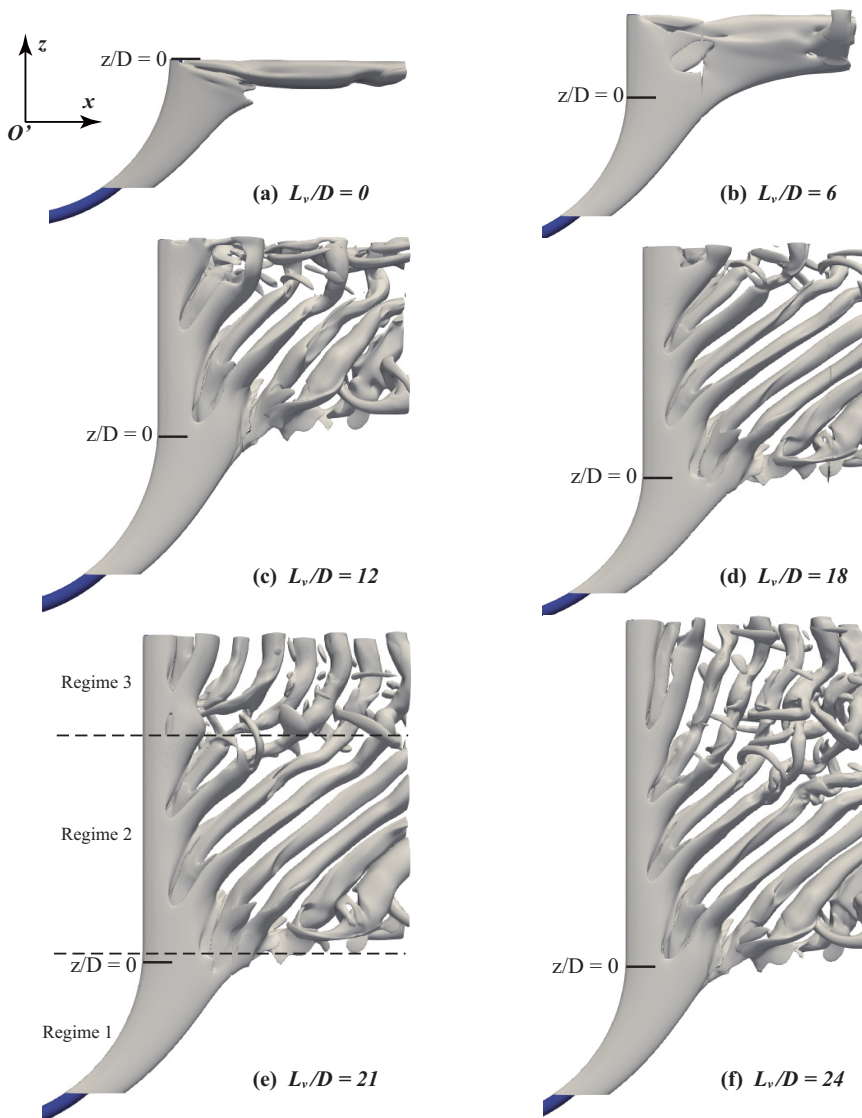


FIG. 4. The wake structure of different VE-simulations, visualized by the iso-surface of $\lambda_2 = -0.01$. All snapshots are viewed in the $+y$ direction. The coordinate system is sketched in (a). Note that O' is not the true origin of the domain. Since each snapshot has a different scale, we indicate $z/D = 0$, i.e., the interface between the curved part and the vertical extension, with a short horizontal solid line in each subplot. The dashed lines in (e) separate the different flow regimes. $Re = 200$.

free-slip boundary condition at the top end prevents the vertical velocity component to penetrate it. Therefore, the wake in Fig. 4(a), i.e., without any vertical extension, is deemed unrealistic.

In Fig. 4(b) one still cannot observe vortex shedding although a $6D$ long vertical extension is appended. Since $Re = 200$ is well beyond the limit at which one should expect vortex shedding ($Re \gtrsim 50$) behind an independent straight cylinder, what is shown in Fig. 4(b) strongly implies that the axial flow plays an important role in the wake behind the vertical extension. It is worth mentioning that, in Ref. [4], the wake exhibited vortex shedding at $Re = 100$ when the $6D$ vertical extension was appended. The reason for this difference is that the axial flow at $Re = 200$ is stronger

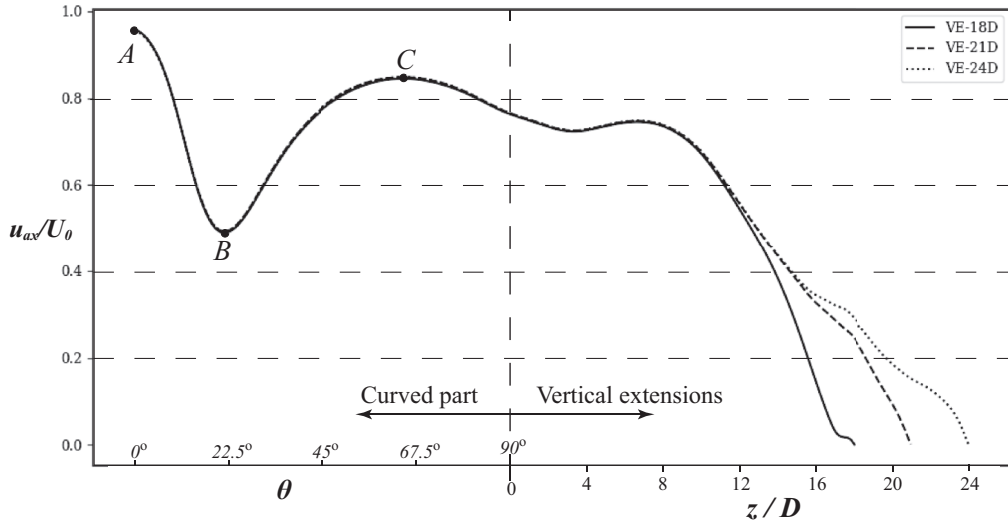


FIG. 5. Comparison of the axial velocity u_{ax}/U_0 distribution along a concentric arc of the curved cylinder, whose radius is $13.6D$, i.e., $0.6D$ behind the cylinder. Results from case VE-18D, VE-21D, and VE-24D are plotted. The abscissa is divided into two parts: the curved part is scaled by the angle θ , while the vertical part is scaled by height z/D . $Re = 200$.

than that at $Re = 100$, which will be shown in the next section (Fig. 12). Nevertheless, Fig. 5 gives an impression of the strong axial flow in the wake for $Re = 200$, though the results are from simulations with longer vertical extensions. For the three VE cases shown in Fig. 5, we observe that at $z/D = 6$ (the top boundary for the VE-6D case), the axial velocity is still at a high level, approximately 75% of the inflow velocity. It is not until after $z/D \approx 9$ (high up in the vertical extension), that the axial velocity starts to drop rapidly. Notice that Fig. 5 is not plotted over the same arc curve as in Fig. 3 ($0.6D$ compared to $1D$ behind the cylinder). Similar conclusions can also be drawn from Fig. 6, in which the time-averaged vertical velocity $\langle w \rangle / U_0$ contours in the symmetry plane from three different VE cases are plotted together for comparison.

Different from VE-0D and VE-6D, the other four VE cases all have clear vortex shedding in the wake, as shown in Figs. 4(c)–4(f). The wakes in VE-21D and VE-24D have the feature of different flow regimes, as mentioned in the Introduction. The three distinct regimes are distinguished in Fig. 4(e) by dashed horizontal lines. It is worth mentioning that regime 3 in Refs. [5,6] was referred to as “normal shedding regime.” We however prefer to call regime 3 in Fig. 4(e) a *slightly oblique shedding* regime, in contrast to the *highly oblique shedding* regime 2, because the vortex filaments in regime 3, as shown in Figs. 4(e) and 4(f), do not align exactly in the spanwise direction of the local straight cylinder. Nevertheless, the different appearances of the two flow regimes are clear.

The three flow regimes also help to understand the interesting axial velocity trends shown in both Fig. 3 (at $Re = 500$) and Fig. 5 (at $Re = 200$). The velocity plot can be characterized by the three markers A, B, and C, indicating different axial positions, in Fig. 5. From A to B, the axial velocity (u_{ax}) experiences a dramatic decrease, while it increases from B to C. This is directly associated with the different wake dynamics in the different flow regimes.

Figure 7 shows the mean axial velocity u_{ax}/U_0 and the two time-averaged velocity components $\langle u \rangle$ and $\langle w \rangle$ along the same concentric arc as in Fig. 5. The results are taken from simulation VE-24D. Notice that the mean crossflow velocity component $\langle v \rangle$ is everywhere zero in the symmetry plane. Marker A indicates the end of the horizontal extension and the start of the curved part. Soon after A, we enter the wake of the cylinder. The continuously decreasing $\langle u \rangle / U_0$ in Fig. 7 is an

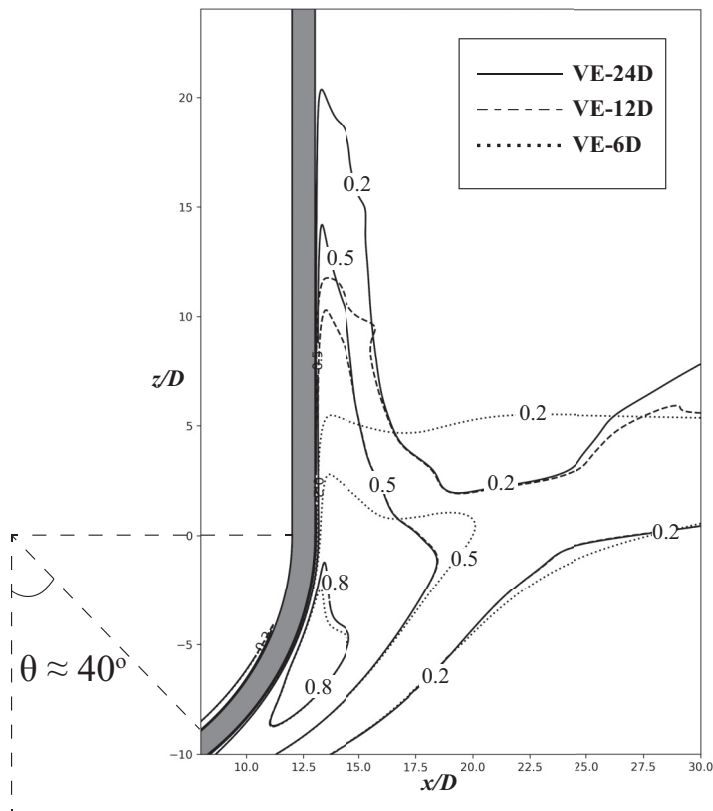


FIG. 6. Results of the time-averaged vertical velocity $\langle w \rangle / U_0$ contours in the symmetry plane for three cases (VE-24D, VE-12D, VE-6D) are plotted together for comparison. For each case, the contours of $\langle w \rangle / U_0 = 0.2, 0.5, 0.8$ are plotted. $Re = 200$.

indication of the shelter effect of the cylinder. When θ is small, $\langle u \rangle$ is the main component of u_{ax} , therefore the axial velocity follows closely the $\langle u \rangle$ curve until it reaches the location B. From B to C, although $\langle u \rangle$ continues to decrease, the axial velocity increases, mainly due to the increase of the vertical velocity component $\langle w \rangle$. The increase of $\langle w \rangle$ is induced by the rolling up of a counter-rotating vortex pair in regime 1. Due to the curved separation lines, a vorticity component normal to the separation line is generated during the separation, and the production of this vorticity component leads to an increased $\langle w \rangle$. A detailed description of this process can be found in Ref. [23]. The velocity component $\langle w \rangle$ stops to increase at around $\theta = 70^\circ$ and decreases slowly afterwards. This is apparently an influence of the vortex shedding in regime 2, in which the production process of $\langle w \rangle$ is suppressed. The axial velocity reaches its peak value at C, somewhat earlier than where $\langle w \rangle$ starts to decrease, simply because of the decreasing velocity component $\langle u \rangle$. By observing Figs. 4(e) and 4(f), we have the impression that regime 2 begins at around $z/D = 0$. This agrees with the results in Fig. 7, in which we see the $\langle u \rangle$ value drops below 0 at around $\theta = 85^\circ$ (close to $z/D = 0$), as a result of the recirculation region associated with the vortex shedding in regime 2.

Here we would like to comment that although we see almost parallel vortex shedding close to the top boundary in Figs. 4(c) and 4(d), we attribute this to the influence of the free-slip boundary condition, which fixes $w = 0$ and $\partial u / \partial z = \partial v / \partial z = 0$ at the top boundary. Therefore, the vortex filaments are forced to be perpendicular to the top boundary. In other words, we cannot trust the results very close to (roughly within $2D$ from) the top boundary. This applies to VE-21D and VE-24D as well. Nevertheless, we can still identify, from Fig. 4, where regime 2 changes to a different

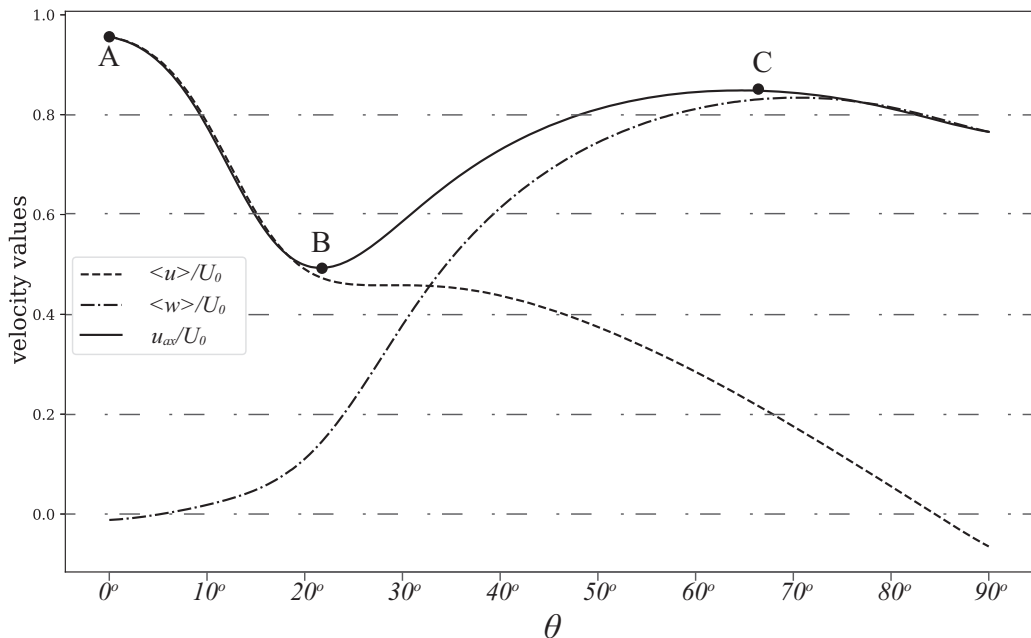


FIG. 7. The time-averaged streamwise velocity $\langle u \rangle / U_0$, vertical velocity $\langle w \rangle / U_0$, and the axial velocity u_{ax} / U_0 along the same concentric arc for the curved part of the cylinder, similarly as in Fig. 5. Results taken from simulation VE-24D, at $Re = 200$.

regime, and treat it as a boundary of different flow regimes, only to compare with the VE-21D and VE-24D results. The idea is applied in Fig. 8, where the location of the interfaces between different flow regimes (both between regimes 1 and 2, and between regimes 2 and 3) are plotted for VE-12D, VE-18D, VE-21D, and VE-24D, respectively. The boundaries in Fig. 8 is based on observations only, since there is no precise definition of where the flow regimes change.

As mentioned in the Introduction, oblique shedding is induced by 3D effects. We have already observed the strong axial flow behind the curved part of the cylinder in Fig. 5, as well as in the contour plots in Fig. 6. This axial flow clearly serves as a trigger for the strongly oblique shedding in regime 2. The 3D effect that triggers the slightly oblique shedding in regime 3 is, however, not obvious. In Fig. 8 we notice that regime 2 begins at about the same location $z/D \approx 0$ for all four cases at $Re = 200$ (later we will show that the inception of regime 2 is Re -dependent, e.g., in Fig. 11), which means these simulations give similar flow field results behind the curved part of the cylinder. However, the location of the boundary between regimes 2 and 3 varies a lot. It locates at $z/D \approx 10$ for case VE-12D, while at $z/D \approx 16$ for case VE-18D. In both cases, the flow pattern experiences abrupt changes at a distance $2D$ below the top boundary. In other words, it is reasonable to assume that the direct influence of the top boundary condition spreads down a distance $2D$. For VE-21D and VE-24D, however, we observe that the boundary between regimes 2 and 3 are both at $z/D \approx 16.5$, which delivers two messages:

- (1) We can assume that, at $Re = 200$, the boundary between regimes 2 and 3 (at $z/D \approx 16.5$) will not change even if L_v extends beyond $24D$.
- (2) The axial flow also affects regime 3, because we see from Fig. 5 that $\langle w \rangle$ can still be as large as $0.2U_0$ at $z/D = 20$, which is more than $3D$ up into regime 3. This axial flow is the reason why the slightly oblique shedding, instead of normal parallel shedding, is observed in regime 3.

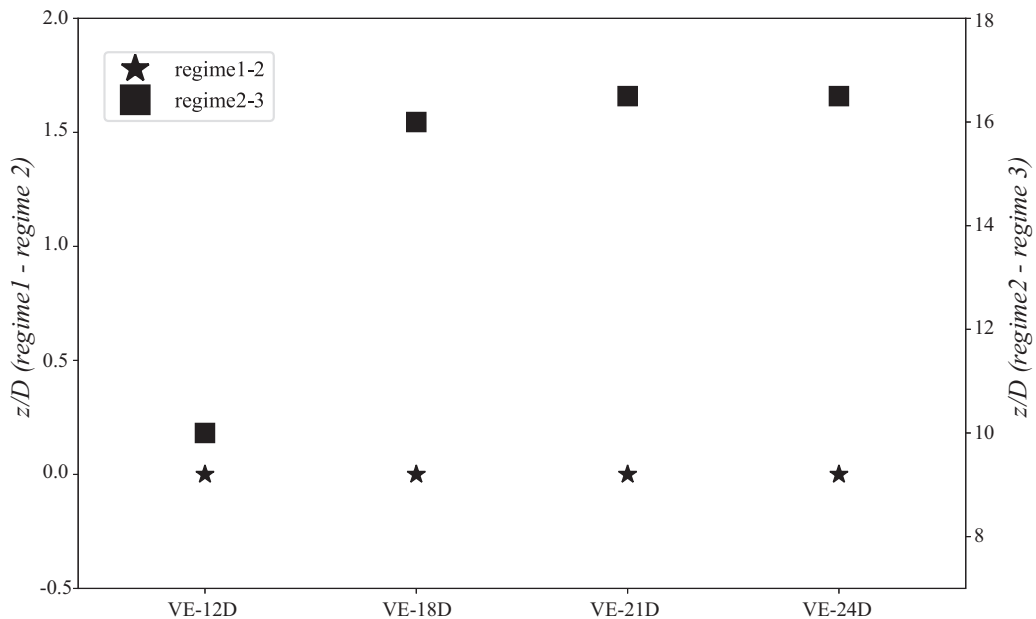


FIG. 8. The location of the boundaries between adjacent regimes. Left ordinate for the boundary between regime 1 and 2, right ordinate for that between regimes 2 and 3.

Figure 9 shows the power spectrum density distribution of the cross-flow velocity component v along a vertical sampling line in the vertical extension wake for two representative cases, VE-12D and VE-24D, respectively. The sampling line is in the symmetry plane and $3D$ behind the cylinder, as sketched in Fig. 9(c). In Fig. 9(a) we can spot only one dominating frequency component $St_1 = f_1 D/U_0 = 0.126$. This frequency is considerably lower than the generally known vortex shedding frequency behind a straight circular cylinder at $Re = 200$ (normally 0.18–0.19). But such a low frequency is not surprising since one easily notices, in Fig. 4, the relatively large shedding angle in regime 2. The relationships between the frequency and the oblique shedding angle will be discussed later in Sec. IV B. St_1 can be detected for all VE cases in regime 2. Therefore, f_1 is directly associated with the strong oblique shedding in this wake. Similar large shedding angles are also reported in Ref. [5], although its experimental research considered different configurations (radius of curvature $R/D = 19$ and 38 , compared to $R/D = 12.5$ in the present study).

In Fig. 9(b) we observe another dominating frequency $St_2 = f_2 D/U_0 = 0.172$ at higher z/D locations. f_2 first appears at around $z/D = 15$ but the energy is low, and it gradually becomes dominating as we move into regime 3. This frequency is much higher compared to f_1 , but still slightly lower than a normal shedding frequency at $Re = 200$, which again indicates that the vortex shedding in regime 3 is not parallel.

From the above discussions, we found that the vertical extension, which had not been carefully exploited before, has significant influence on the wake behind a concave curved cylinder. The axial flow behind the curved cylinder triggers a strongly oblique shedding in a certain region (referred to as regime 2). This strongly oblique shedding switches to a slightly oblique shedding as the axial flow gradually fades away. We do not observe an exact parallel shedding in this series of simulations. We observe that the shift between regime 2 and 3 locates identically at $z/D \approx 16.5$ in both VE-21D and VE-24D cases, which means the vertical extension length influence has “saturated” when $L_v = 24D$ at this Reynolds number. The wake in the VE-24D case can be divided into three regimes, namely, a nonshedding regime 1, a strongly oblique shedding regime 2, and a slightly oblique shedding regime 3. The dominating frequencies for regime 2 and regime 3 are $St_1 = 0.126$ and $St_2 = 0.172$,

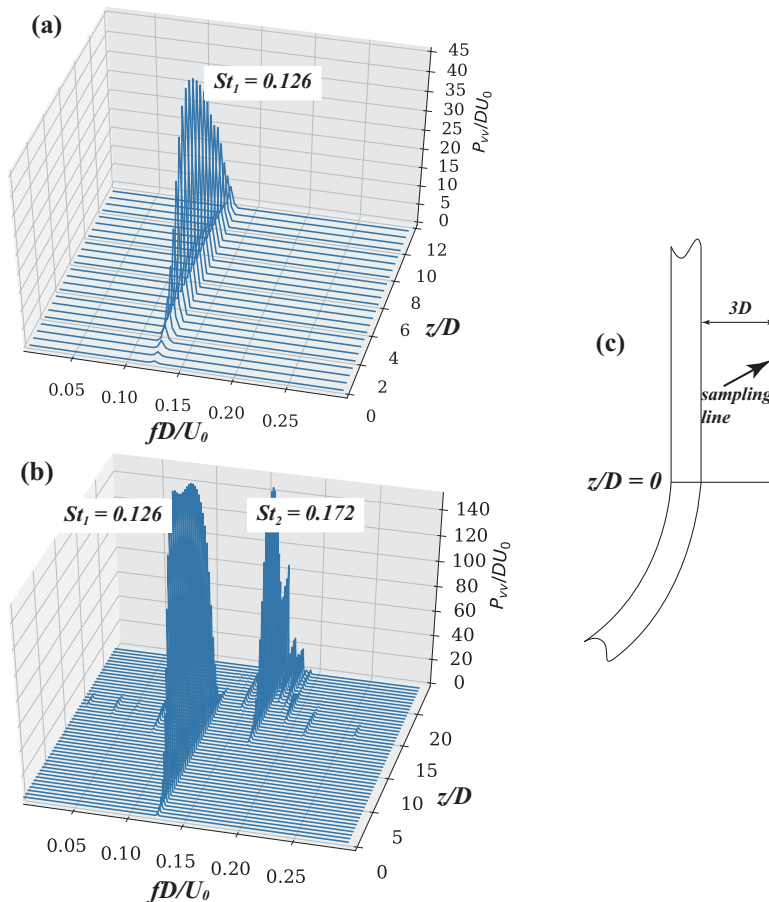


FIG. 9. Power spectrum density distribution of the cross-flow velocity v along a sampling line $3D$ behind the vertical extension in the symmetry plan ($y/D = 0$), as sketched in (c). (a) VE-12D, (b) VE-24D. The main frequencies are indicated. $Re = 200$.

respectively. Both are lower than the parallel shedding frequency behind a straight cylinder at $Re = 200$. We have attributed the appearance of the oblique shedding in both regimes to the 3D effect caused by the axial flow. It is possible that truly parallel vortex shedding will appear when L_v becomes even longer and that the vertical velocity eventually decays to zero, as also will be commented in Sec. IV B.

IV. THE CONCAVE CURVED CYLINDER WAKE AT DIFFERENT Re

A. Wake transition

In this section, we present the wake flow results obtained from a series of simulations of the concave curved cylinder at different Reynolds numbers, ranging from $Re = 100$ to 500 . The detailed information is listed in Table I as the “Re series.” We directly adopt $L_v = 24D$ from the above discussions for all the Re-effect cases. The minimum grid sizes were chosen based on the conclusions from the earlier grid study (in Sec. II C).

Figure 10 shows snapshots of λ_2 rendering, namely, the instantaneous vortical structures in the wake, at four different Re : 100, 200, 300, and 500, respectively. Notice that Figs. 10(a) and 10(b) use the same color map scale, while 10(c) and 10(d) use a different scale. This is to make all the wake

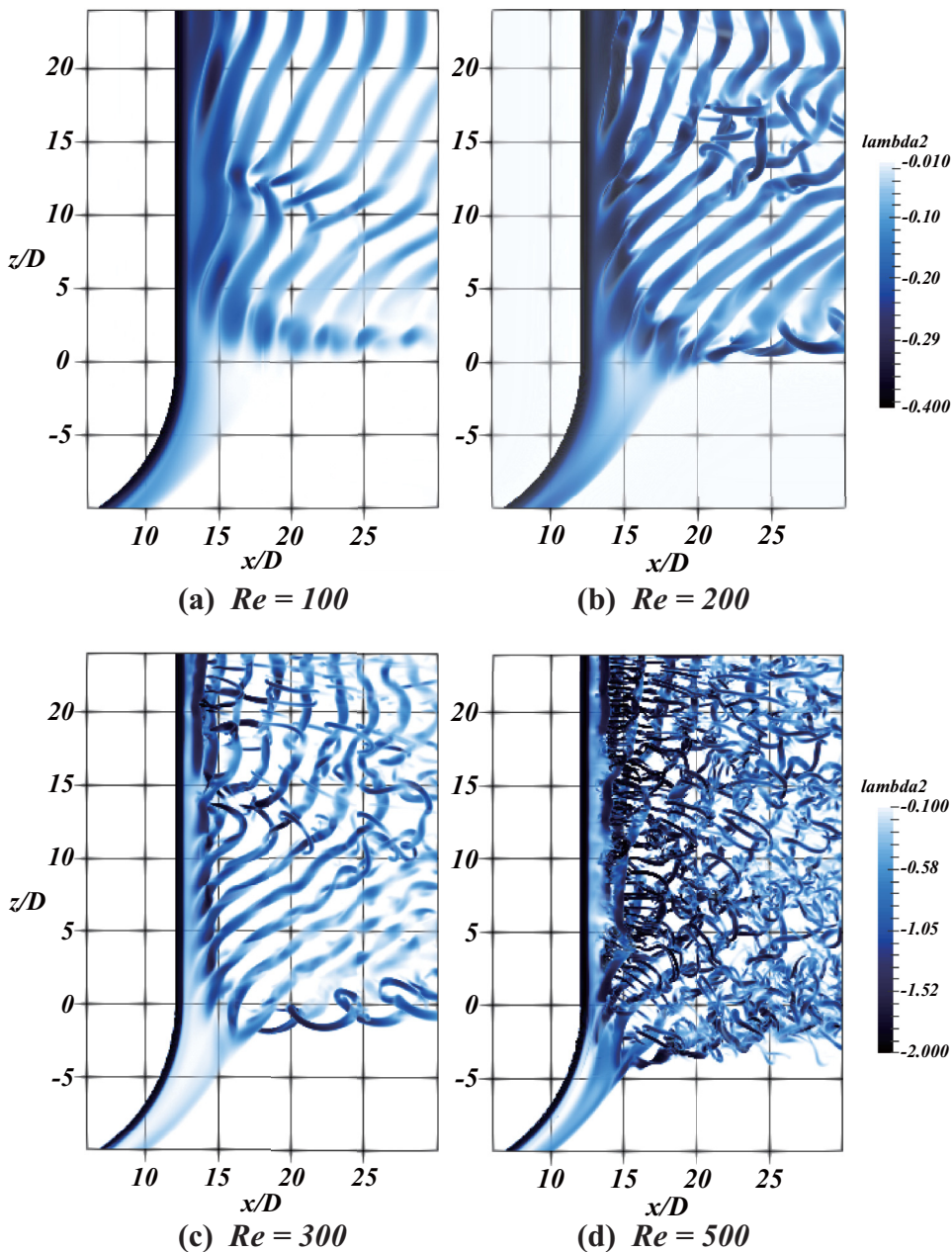


FIG. 10. The rendering of λ_2 , showing instantaneous wake snapshots at (a) $Re = 100$, (b) $Re = 200$, (c) $Re = 300$, and (d) $Re = 500$, respectively. All snapshots are viewed in the $+y$ direction, and $L_v = 24D$. Notice that (a) and (b) use the same color map scale indicated in (b), while (c) and (d) use the different color map scale indicated in (d).

structures visible in each plot. For $Re = 400$, the wake topology is similar to that for $Re = 500$, therefore it is not shown in Fig. 10.

In Fig. 10(a), i.e., at $Re = 100$, the vortex filaments shed regularly. This is a Reynolds number where 3D instabilities do not develop even behind a straight cylinder [8]. In Fig. 10(a) we can

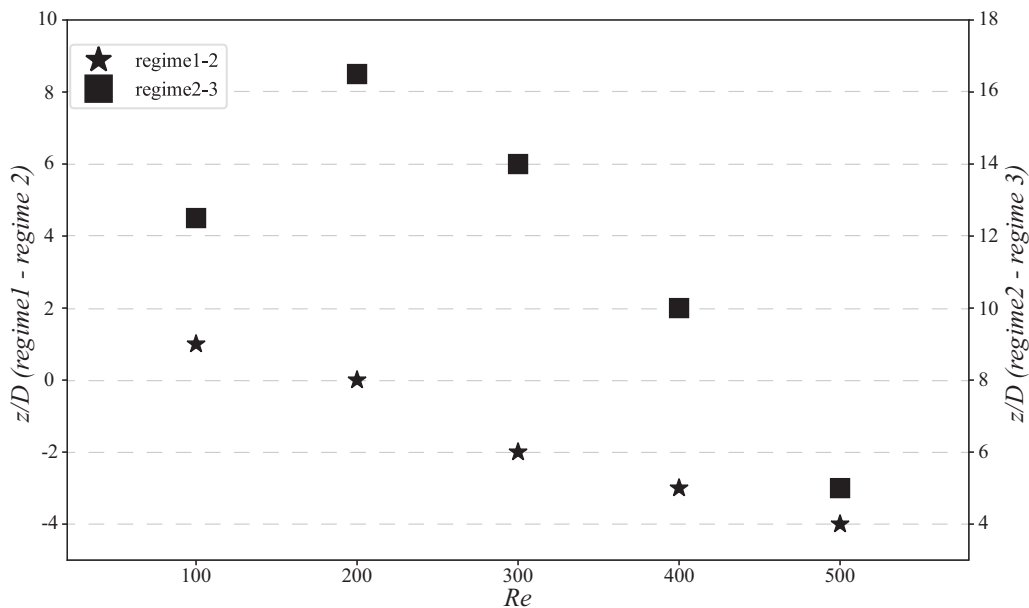


FIG. 11. Locations of the boundaries between different flow regimes at different Re . To read the boundary location between regimes 1 and 2, one uses the left vertical axis, while the right vertical axis is used to read the boundary location between regimes 2 and 3.

roughly outline two different shedding regimes, of which one is slightly more oblique, i.e., the so-called regime 2. The difference between the two flow regimes is not as clear as in Figs. 10(b)–10(d), where the strong oblique shedding regime 2 is clearly visible. However, we could still spot two different shedding regimes by the complex structures at the boundary of the two regimes in Fig. 10(a). These structures indicate the vortex dislocation phenomenon, which normally happens at the boundary between two flow regions that have different dominating frequencies [7]. At $Re = 200$, i.e., in Fig. 10(b), we observe a more complex vortex dislocation phenomenon at the boundary between regimes 2 and 3. The primary 3D instabilities, i.e., mode A as proposed in Ref. [8], are barely visible in regime 3. At $Re = 200$, the 3D instability should already appear in a straight cylinder wake, but will be delayed when the shedding is oblique [7].

In Fig. 10(c), at $Re = 300$, the 3D instabilities become clear in regime 3, represented by the streamwise vortical structures bridging adjacent axial vortex filaments. However, we still could not observe similar instabilities in regime 2, although in the more downstream part, the oblique vortex filaments start to become wavy. When we look at the $Re = 500$ case in Fig. 10(d), the whole flow field is apparently more complex with massive fine vortical structures.

Based on the results in Fig. 10, we can again map the location of the boundaries between different flow regimes for different Re . This is shown in Fig. 11. As Re increases, the wake gets more unsteady, therefore we can intuitively anticipate that vortex shedding would develop earlier (at a lower z position in this context) at larger Re . This is seen by the continuous decrease of the boundary locations between regime 1 and regime 2 in Fig. 11. The oblique shedding occurs at $z/D \approx 1$ at $Re = 100$, but at $z/D \approx -4$ at $Re = 500$.

It should be noticed that the oblique vortex shedding in Figs. 10 and 11 occurs behind the straight vertical extension of the concave curved cylinder where $\sin \theta$ is constant and equal to 1 [see Fig. 1(b)]. The hypothesized analogy between wakes behind tapered cylinders [11], cylinders in shear flow [10], and curved cylinders cannot explain the present findings since the oblique shedding is observed behind the straight vertical extension. However, the results in Fig. 11 indicate that the emergence of oblique shedding shifts downwards and into the curved part of the concave cylinder

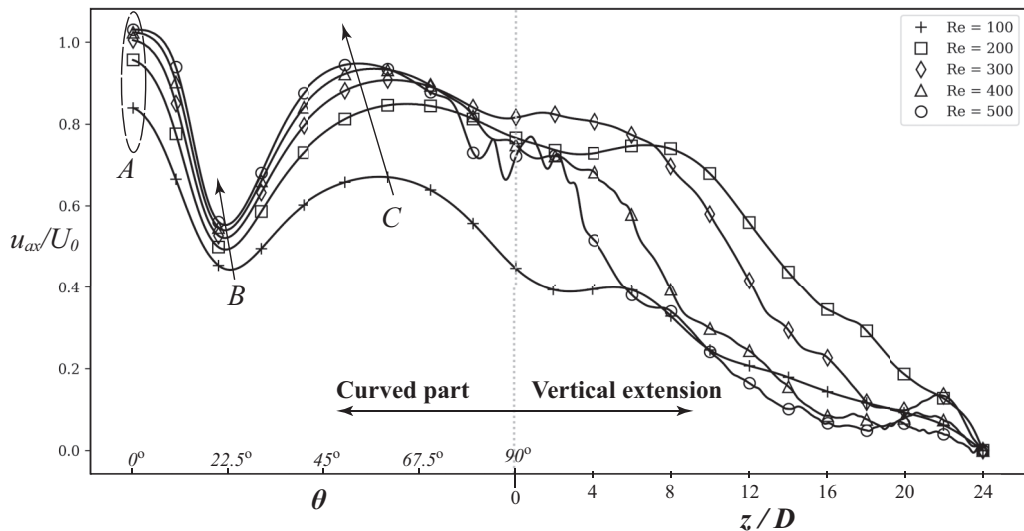


FIG. 12. The axial velocity distribution u_{ax}/U_0 following the axial direction of the cylinder, both the curved part and the vertical extension part, $0.6D$ behind the leeward side of the cylinder surface. The abscissa is arranged in the same way as in Fig. 5. Results for all five Re are plotted. The arrows show the tendency when Re increases. $L_v/D = 24$.

configuration as Re increases. The validity of the suggested analogy can probably be examined at even higher Re .

Differently from the clear trend of the inception location of regime 2 as Re increases, the end location of regime 2 is, however, more complex. We notice that the upper boundary of regime 2 first increases from $z/D \approx 12.5$ at $Re = 100$ to $z/D \approx 16.5$ at $Re = 200$, but then experiences a decrease all the way to $z/D \approx 5$ at $Re = 500$. To understand this interesting phenomenon, we need to investigate the axial velocity distribution close to the geometry. Figure 12 plots the time-averaged axial velocity u_{ax} distribution along a line $0.6D$ behind the cylinder surface, the same as in Fig. 5, for all five Re values. This line starts from the inception of the curved part and ends at the top boundary.

We notice that behind most of the curved part of the cylinder, the mean axial velocity is monotonically increasing as Re increases. This tendency applies up to $\theta \approx 67.5^\circ$, at which the u_{ax}/U_0 distributions for $Re = 400$ and 500 experience a relatively sharp decrease and become more unstable, and soon drops below the $Re = 200$ and 300 distributions. This corresponds to the appearance of vortex shedding at these two Reynolds numbers. The velocity distributions for $Re = 200$ and 300 continue to be relatively smooth up to the vertical extension part. The mean axial velocity at $Re = 300$ is higher than that at $Re = 200$ all the way up to $z/D \approx 7$, where it suddenly drops below that at $Re = 200$. Thereafter, we clearly notice that the axial velocity at $Re = 200$ is the largest among all five cases. The oblique shedding happens due to the production of streamwise vorticity, and the higher the streamwise vorticity is compared to the axial vorticity, the larger the oblique shedding angle will be. In general, higher axial velocity levels induce higher streamwise vorticity. Therefore, it is the highest axial velocity values at $Re = 200$ that prevent the strongly oblique shedding in regime 2 to shift to a slightly oblique shedding, so we see the peak point at $Re = 200$ in Fig. 11. We would like to mention here, that the strongly oblique shedding comprises the largest territory (ranging from $z/D = 0$ to 16.5) at $Re = 200$, which was also the main reason why we considered $Re = 200$ for the vertical extension length test.

In Fig. 12 we also notice that the axial velocity is dramatically lower at $Re = 100$ compared to the other four Re , at which the velocity values are roughly the same when regime 2 begins (between

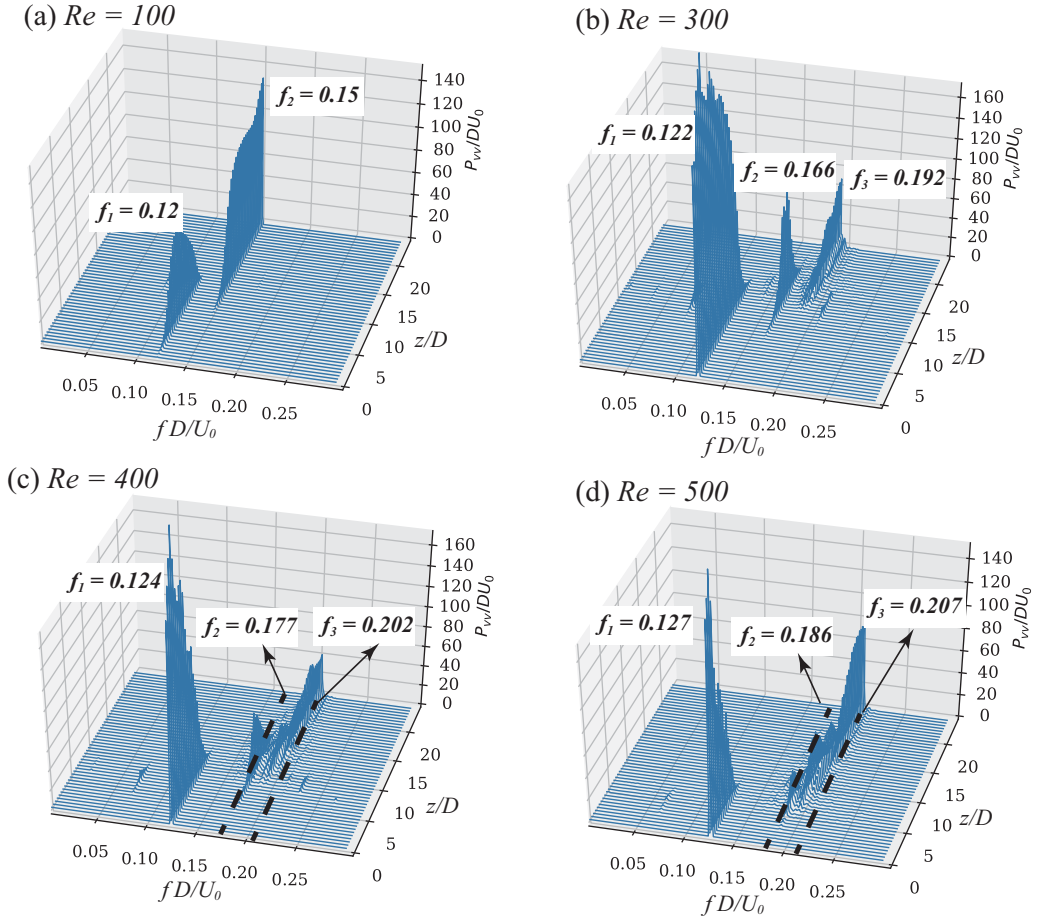


FIG. 13. The cross-flow velocity energy spectrum plotted over a vertical line at $x/D = 16$, $y/D = 0$, and over a vertical span from $z/D = 0$ to 24, i.e., a vertical line $3D$ behind the vertical extension and in the symmetry plane. Results at (a) $Re = 100$, (b) $Re = 300$, (c) $Re = 400$, and (d) $Re = 500$. The frequency values are marked in each subplot.

$\theta \approx 67.5^\circ$ and 90°). This is somewhat important information in order to explain the clearly lower shedding angle (in regime 2) in Fig. 10(a) compared to Figs. 10(b)–10(d), where the shedding angles are close to each other but larger than that at $Re = 100$. Moreover, in Fig. 12, we observe that the locations B and C, as discussed in Fig. 7, vary with the Re .

B. The frequencies

Figure 13 shows the energy spectrum of the cross-flow velocity v plotted over the same vertical sampling line defined in Fig. 9(c), but for the four other $Re = 100, 300, 400$, and 500 , respectively. The results for $Re = 200$ were plotted in Fig. 9(b), therefore not repeated. By observing the 3D spectrum at different Re , we can divide them into three types:

Type 1: $Re = 100$ and $Re = 200$, characterized by two dominating frequencies, marked as f_1 and f_2 , respectively.

Type 2: $Re = 300$, characterized by three dominating frequencies, marked as f_1 , f_2 , and f_3 , respectively.

TABLE III. The frequency components in the wake at different Re.

Re	f_R^a	f_1	f_1/f_R	f_2	f_2/f_R	f_3	f_3/f_R
100	0.16–0.17	0.12	0.706–0.75	0.15	0.882–0.938	–	–
200	0.18–0.19	0.126	0.663–0.70	0.172	0.905–0.956	–	–
300	0.203	0.122	0.601	0.166	0.818	0.192	0.946
400	0.205	0.124	0.605	0.177	0.863	0.202	0.985
500	0.206	0.127	0.617	0.186	0.903	0.207	1.005

^a f_R : reference value [24] of the shedding frequency in a straight cylinder wake.

Type 3: Re = 400 and Re = 500, characterized by one dominating frequency f_1 , and a frequency band in which the frequency has a “continuous” variation along the z direction. To discuss type 3 together with the other two types, we mark the lower and upper boundaries of the frequency band [indicated by two dashed lines in Figs. 13(c) and 13(d)] as f_2 and f_3 , respectively.

All the frequencies are summarized in Table III, in which the reference frequency f_R indicates the shedding frequency in a straight circular cylinder wake at the corresponding Re. f_R values are taken from Fig. 4.5 in Ref. [24].

For all five Re, f_1 has the same meaning, i.e., the frequency of the highly oblique shedding in regime 2. f_1/f_R at Re = 100 and 200 are approximately 0.7, indicating a mild oblique angle, especially at Re = 100. This agrees with the observations in Fig. 10. f_1/f_R at Re = 300–500 are close to each other (all around 0.6), indicating that the oblique angle in regime 2 at these Reynolds numbers are close. This is again in agreement with the plots in Fig. 10.

From Table III we observe that f_2 at Re = 100 and 200 and f_3 at Re = 300–500 are the highest detected frequencies at the corresponding Re. We notice that f_2/f_R at Re = 100 and 200, and f_3/f_R at Re = 300 are 5%–10% below 1.0, indicating a slightly oblique shedding instead of a parallel shedding. “Slightly” means that the oblique angle is small, compared to the strongly oblique shedding in regime 2. However, f_3 at Re = 400 and 500 is almost identical with f_R , meaning that at these two Re, the vortex shedding becomes parallel to the cylinder axis as we move towards the end of the vertical extension.

The f_2 component at Re = 300, 400, and 500 is more complex. At Re = 300, f_2 stands as a single dominating frequency, while at Re = 400 and 500, f_2 represents the lower boundaries of the “frequency bands” [depicted in Figs. 13(c) and 13(d)]. Despite of this difference, the existence of f_2 tells us that there exist more than two shedding regimes in the concave curved cylinder wake. This is most clearly seen at Re = 300, as plotted in Fig. 14. From this figure, we observe that the wake can be divided into four flow regimes, among which three have vortex shedding. This agrees with the results in Table III. If we assume that the three shedding regimes (regime 1 has no vortex shedding, and thus has no frequency) are directly related to the three dominating frequencies in Table III, we can estimate the oblique angle in each regime based on the frequencies, as indicated in Fig. 14. Three lines (the red dashed lines in Fig. 14) can therefore be drawn based on the estimated oblique angles α_1 , α_2 , and α_3 . We notice that the inclination of the vortical structures in each flow regime agrees well with the three lines, at least in the near wake. In this way, we show that at Re = 300, three distinct shedding regimes can be detected, different from the two shedding regimes at Re = 200, while a nonshedding regime exists at both Re.

However, the scenario at Re = 400 and 500 becomes different. In Fig. 10(d), except for the strongly oblique shedding in the lower wake, we can hardly distinguish other distinct flow regimes like those in Fig. 14. This is consistent with the results in Fig. 13(d). The frequency band, instead of an independent dominating frequency, tells us that at Re = 500 (also 400), the frequency changes along the axial direction in a continuous manner. At Re = 100–300, however, the frequency changes along the axial direction in a stepwise manner. Similar frequency bands were reported in Ref. [9], where they studied cellular vortex shedding behind a tapered circular cylinder and compared it with

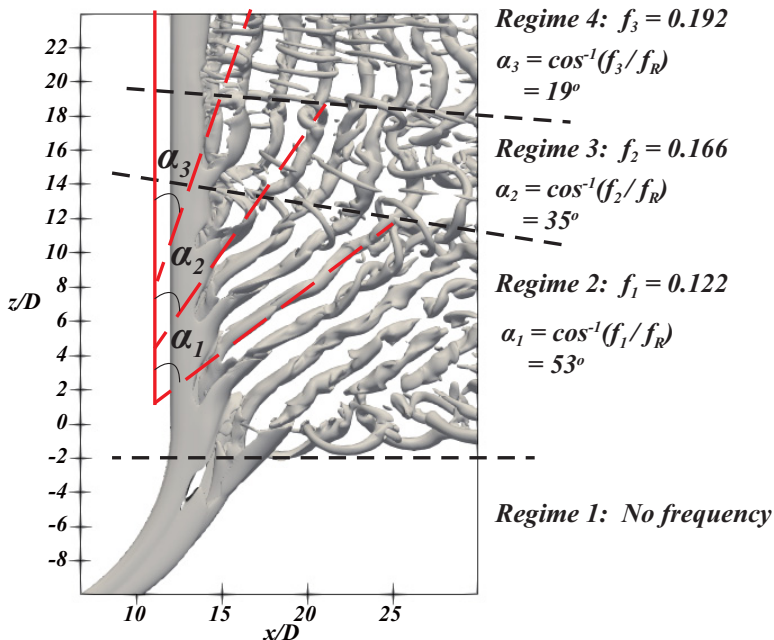


FIG. 14. The wake structure at $Re = 300$ is described by the iso-surface of $\lambda_2 = -0.2$. The four flow regimes are separated by the black dashed lines. The red dashed lines are drawn based on the calculated oblique angles (α_1 , α_2 , and α_3) indicated.

the wake of a circular cylinder in shear flow. Yet one should keep in mind that the local Reynolds number along the cylinder span in Ref. [9] changes as either the cylinder diameter (for tapered cylinder) or the inflow velocity (for shear flow). In the present study, however, the local Reynolds number along the vertical extension is always identical. It shows again the strong effect from the axial flow coming from the curved part of the cylinder.

At last, we note that parallel vortex shedding is observed at $Re = 400$ and 500 , but not at lower Re , because the axial velocity drops faster as we move towards the vertical extension at higher Re (as discussed in conjunction with Fig. 12). We suspect that the axial velocity eventually will disappear even at lower Re , provided that the vertical extension is infinitely long, and the vortex shedding will become parallel (when the extension is sufficiently long). However, this is out of the scope of the present study and clearly needs more simulations to investigate.

V. CONCLUDING REMARKS

We presented a detailed investigation, by means of a series of direct numerical simulations, of the wake flow behind an $R/D = 12.5$ quarter-of-ring concave curved cylinder, with horizontal and vertical extension appended to its two ends.

The length effect of the vertical extension, i.e., the VE series, was first addressed, and turns out to be significant to the wake flow. We fixed $Re = 200$ for the VE study. When the vertical extension length $L_v \leq 6D$, no vortex shedding exists in the wake. The wakes of the VE-12D and VE-18D configurations have strongly oblique vortex shedding but are still heavily influenced by the upper free-slip boundary. The oblique shedding in the concave curved cylinder wake is caused by the strong axial flow in the near wake. It is not until L_v is increased to $21D$ and $24D$ that we start to notice a convergence trend. Three flow regimes, i.e., the nonshedding regime 1, the strongly oblique shedding regime 2, and the slightly oblique shedding regime 3, can be identified in both the VE-21D wake and the VE-24D wake. The boundary between regime 2 and 3 no longer varies as L_v

increased from $21D$ to $24D$. We therefore conclude that one may need at least a $21D$ long vertical extension at $Re = 200$ to get a reliable wake for this configuration. Although a parallel shedding regime is not observed in the VE studies, as proposed in earlier studies [5], we would expect it to appear if the vertical extension is further increased (and the axial velocity disappears). In the present study, we have observed that the axial velocity can be as high as 20% of the free-stream velocity U_0 at $z/D = 20$, at $Re = 200$. Therefore even for the longest vertical extension case VE-24D, we still have an axial flow influence. This is somewhat surprising because earlier curved cylinder wake studies, although at different Re , used much shorter vertical extension lengths. The effect of the vertical extension has most likely been underestimated before.

We studied the transition scenario in this concave curved cylinder wake flow, through the Re-series simulations, and found that the vertical extension length effect is Re-dependent, as shown in Fig. 11. The most demanding Reynolds number with respect to the vertical extension length is $Re = 200$. As Re increases, the wake experiences similar 3D instabilities as in the straight circular cylinder wake, but the oblique shedding postpones the transition.

The 3D velocity energy spectra in Fig. 9 and Fig. 13 reveal three distinct types of wake within a narrow Re range from 100 to 500. Together with the snapshots of the wake structures in Fig. 10 and Fig. 14, we show that more than two shedding regimes may coexist in a concave curved cylinder wake. While the strongly oblique shedding is a direct result of the nonshedding regime (dominated by a counter-rotating vortex pair and generation of strong axial flow), it can be observed at all Re considered in the present study. We have also discussed that a parallel shedding regime must appear, provided that the vertical extension is sufficiently long. Moreover, slightly shedding regimes may exist in between these two regimes, as is most clearly seen at $Re = 300$, where three distinct dominating frequencies are detected instead of only two.

It is furthermore interesting that we have observed two different manners by which the strongly oblique shedding switches to a parallel shedding. At $Re \leq 300$, this process takes place stepwise, while at $Re = 400$ and 500 , this process takes place continuously. The latter of which is supported by the appearance of a frequency band in Figs. 13(c) and 13(d) instead of an isolated dominating frequency in Fig. 13(b).

ACKNOWLEDGMENTS

This study was supported by the Future Industry's Leading Technology Development program (No. 10042430) of MOTIE/KEIT of Korea. The work has also received support from the Research Council of Norway (Program for Supercomputing, under project *nn9191k*) through a grant of computing time.

-
- [1] J. P. Gallardo, B. Pettersen, and H. I. Andersson, Turbulent wake behind a curved circular cylinder, *J. Fluid Mech.* **742**, 192 (2014).
 - [2] T. Leweke and M. Provansal, The flow behind rings: Bluff body wakes without end effects, *J. Fluid Mech.* **288**, 265 (1995).
 - [3] A. Miliou, S. J. Sherwin, and J. M. R. Graham, Fluid dynamic loading on curved riser pipes, *Trans. ASME: J. Offshore Mech. Arctic Eng.* **125**, 176 (2003).
 - [4] A. Miliou, A. de Vecchi, S. J. Sherwin, and J. M. R. Graham, Wake dynamics of external flow past a curved circular cylinder with the free stream aligned with the plane of curvature, *J. Fluid Mech.* **592**, 89 (2007).
 - [5] J. K. Shang, H. A. Stone, and A. J. Smits, Flow past finite cylinders of constant curvature, *J. Fluid Mech.* **837**, 896 (2018).
 - [6] S. Ramberg, The effects of yaw and finite length upon the vortex wakes of stationary and vibrating circular cylinders, *J. Fluid Mech.* **128**, 81 (1983).

- [7] C. H. K. Williamson, Oblique and parallel modes of vortex shedding in the wake of a circular cylinder at low Reynolds numbers, *J. Fluid Mech.* **206**, 579 (1989).
- [8] C. H. K. Williamson, Vortex dynamics in the cylinder wake, *Annu. Rev. Fluid. Mech.* **28**, 477 (1996).
- [9] P. Parnaudeau, D. Heitz, E. Lamballais, and J.-H. Silvestrini, Direct numerical simulations of vortex shedding behind cylinders with spanwise linear nonuniformity, *J. Turbul.* **8**, 13 (2007).
- [10] J. H. Silvestrini and E. Lamballais, Direct numerical simulation of oblique vortex shedding from a cylinder in shear flow, *Int. J. Heat Fluid Flow* **25**, 461 (2004).
- [11] V. D. Narasimhamurthy, H. I. Andersson, and B. Pettersen, Cellular vortex shedding behind a tapered circular cylinder, *Phys. Fluids* **21**, 044106 (2009).
- [12] G. R. S. Assi, N. Srinil, C. M. Freire, and I. Korkischko, Experimental investigation of the flow-induced vibration of a curved cylinder in convex and concave configurations, *J. Fluids Struct.* **44**, 52 (2014).
- [13] A. de Vecchi, S. J. Sherwin, and J. M. R. Graham, Wake dynamics of external flow past a curved circular cylinder with the free-stream aligned to the plane of curvature, *J. Fluids Struct.* **24**, 1262 (2008).
- [14] N. Srinil, B. Ma, and L. Zhang, Experimental investigation on in-plane/out-of-plane vortex-induced vibrations of curved cylinder in parallel and perpendicular flows, *J. Sound Vib.* **421**, 275 (2018).
- [15] J. P. Gallardo, B. Pettersen, and H. I. Andersson, Effects of free-slip boundary conditions on the flow around a curved circular cylinder, *Comput. Fluids* **86**, 389 (2013).
- [16] F. Jiang, B. Pettersen, and H. I. Andersson, Influences of upstream extensions on flow around a curved cylinder, *Eur. J. Mech. B* **67**, 79 (2018).
- [17] M. Manhart, F. Tremblay, and R. Friedrich, MGLET: a parallel code for efficient DNS and LES of complex geometries, in *Parallel Computational Fluid Dynamics—Trends and Applications*, edited by C. B. Jensen, T. Kvamsdal, H. I. Andersson, B. Pettersen, A. Ecer, J. Periaux, N. Satofuka, and P. Fox (Elsevier, Amsterdam, 2001), pp. 449–456.
- [18] J. H. Williamson, Low-storage Runge-Kutta schemes, *J. Comput. Phys.* **56**, 48 (1980).
- [19] H. L. Stone, Iterative solution of implicit approximations of multidimensional partial differential equations, *SIAM J. Numer. Anal.* **5**, 530 (1968).
- [20] N. Peller, A. Le Duc, F. Tremblay, and M. Manhart, High-order stable interpolations for immersed boundary methods, *Int. J. Numer. Meth. Fluids* **52**, 1175 (2006).
- [21] M. Manhart, A zonal grid algorithm for DNS of turbulent boundary layers, *Comput. Fluids* **33**, 435 (2004).
- [22] J. Jeong and F. Hussain, On the identification of a vortex, *J. Fluid Mech.* **285**, 69 (1995).
- [23] F. Jiang, J. P. Gallardo, and H. I. Andersson, The laminar wake behind a 6:1 prolate spheroid at 45° incidence angle, *Phys. Fluids* **26**, 113602 (2014).
- [24] M. M. Zdravkovich, *Flow around Circular Cylinders, Vol. 1: Fundamentals* (Oxford Science Publications, Oxford, 1997).